Optimal Duty Cycle Model Predictive Current Control of High-Altitude Ventilator Induction Motor With Extended Minimum Stator Current Operation

Liming Yan, Manfeng Dou, *Member, IEEE*, Zhiguang Hua, Haitao Zhang, and Jianwei Yang

***Abstract*—High-altitude ventilator has been utilized to blow the air into airship airbags to achieve flight control of the stratospheric airship. Owing to the thin air in the stratosphere, high-altitude ventilator induction motor operates at high-speed light-load condition. The traditional minimum stator current operation is employed to minimize conduction and switching losses below the rated speed. This paper extends this concept to the field-weakening region, and puts forward the extended minimum stator current operation (EMSCO) to obtain high efficiency at any speed. The EMSCO criterion is formalized as constrained optimization problem that is solved by breaking down into subproblems. The proposed EMSCO maps the torque reference onto the optimal field current and torque current references. In addition, optimal duty cycle model predictive current control (ODC-MPCC) is proposed to reduce the current ripple and computation burden compared with traditional MPCC. In ODC-MPCC, the novel cost function based on deadbeat voltage vector reduces the computation burden. The proposed ODC-MPCC of induction motor with EMSCO is verified effectively by simulation and experiment, which is compared with the traditional control strategy of induction motor.**

***Index Terms*—High-altitude ventilator, induction motor, minimum stator current operation, model predictive control.**

I. Introduction

DUE to its long residence time in the stratosphere, large load capacity, and wide coverage, the stratospheric airship is employed in environmental monitoring, relay communication, and scientific detection, which makes it receive more attention in recent years [1]. The high-altitude ventilator is utilized to inject the air into airbag to achieve flight control of the stratosphere airship [2], [3]. The research on the optimized control strategy of high-altitude ventilator is crucial to improve the operation performance and energy saving of airship.

Multidimensional physical parameter modeling and control of high-altitude ventilator is rare in the literature, while the main research focuses on the ground ventilator system. The modeling methods of ground ventilator mainly are divided into curve fitting and neural network [4], [5]. The control strategies of the ground ventilator consists of constant speed control and variable speed control [6]. Constant speed control strategy contains changes of the pipe characteristic curve, the valve adjustment, and inlet guide vane adjustment, which have the features of a simple operation and the low efficiency [7], [8]. The variable speed control strategy is to regulate the ventilator speed to alter the ventilator characteristic curve, and then realize the volume flow control of ventilator. This method has the features of high equipment cost and high efficiency [9].

Because of the thin air at high altitude, high-altitude ventilator needs to increase the rotation speed to meet the demand of static pressure difference between the airbag and atmosphere. In this case, high-altitude ventilator induction motor operates at field-weakening mode and in light-load state. The traditional field-weakening control algorithms of induction motor can be classified into three kinds [10]–[14]. The first algorithm is $1/\omega_r$ field-weakening method, which makes the field current inversely proportional with the speed in the field-weakening mode. This algorithm is easy to implement but cannot obtain the optimal field current with variable load torque. The second algorithm is to calculate the field current and torque current based on the precise mathematical model of induction motor. This algorithm can theoretically obtain the maximum output torque at voltage and current limits, but it heavily depends on induction motor parameters. The third algorithm is to exploit the voltage feedback to adjust field current. This algorithm can obtain maximum torque output capability and is independent on the parameters of induction motor, but the voltage outer-loop controller increases the complexity and instability of the system [15], [16]. Furthermore, it cannot guarantee the optimal operation with minimum stator current when the torque reference is small. In [17], four kinds of field-weakening methods are compared and analyzed in detail. In [18], the constrained maximum torque per ampere (MTPA) criterion of permanent magnet synchronous motor is extended to the weakening region to achieve high efficiency at any speed.

In recent years, finite control set model predictive control (FCS-MPC) has been widely used in power electronics and electric drive [19]–[23]. FCS-MPC adopts discrete optimization method, which selects the optimal voltage by the cost function in one sampling period. This method is consistent with the dis-

Manuscript received May 27, 2017; revised August 27, 2017; accepted September 29, 2017. Date of publication October 5, 2017; date of current version April 20, 2018. Recommended for publication by Associate Editor J. Rodriguez. *(Corresponding author: Liming Yan.)*

The authors are with the Department of Electrical Engineering, School of Automation, Northwestern Polytechnical University, Xi'an 710072, China (e-mail: liming123@mail.nwpu.edu.cn; doumf@nwpu.edu.cn; hzguang@mail.nwpu.edu.cn; zhtshr@163.com; yangjianwei100@hotmail.com).

Color versions of one or more of the figures in this paper are available online at http://ieeexplore.ieee.org.

Digital Object Identifier 10.1109/TPEL.2017.2759906

cretization and nonlinearity of power electronic and electrical drives [24]–[26]. Model predictive current control (MPCC) is first proposed in [27], and then quickly receives more attention due to its straightforward concept and good performance. However, the hard setting of weighting factor, heavy computation burden, and current ripple become obstacles for the development of model predictive control. In [28], multiobjective optimization using fuzzy decision making is proposed to substitute the scalar cost function. In [29], FCS-MPC with a deadbeat solution for permanent-magnet synchronous motor drives is put forward to reduce the candidate voltage vectors. Because of only one voltage vector applied at one sampling period, current ripple is more heavy compared with Space vector pulse width modulation. Some scholars have proposed to employ two voltage vectors with duty cycle to decrease the ripple. In [30], predictive duty cycle control with online optimizing is proposed for rectifier to predict instantaneous current variations. The paper [31] is devoted to put forward a novel duty cycle control strategy to reduce both torque and flux ripples. In [32], two-vector-based model predictive torque control is put forward to decrease torque ripple, and simultaneously this paper adopts predicting stator flux linkage vector leaving out the weigh factor of the cost function.

In this paper, four-dimensional mathematical model of high-altitude ventilator is established, and then the flow tracking control strategy is put forward to achieve volume flow control. The proposed optimal duty cycle model predictive current control (ODC-MPCC) of induction motor with extended minimum stator current operation (EMSCO) not only decreases the stator current, but also lower the computation burden of model predictive control. This paper is arranged as follows: Section II introduces the mathematical model of high-altitude ventilator, flow tracking control strategy, and the load characteristics of ventilator; Section III introduces the extended minimum stator current control strategy; Section IV introduces ODC-MPCC to achieve fast tracking of stator current reference; Section V verifies the effectiveness of the algorithm by simulation and experiment; Section VI presents the conclusion of this paper.

II. High-Altitude Ventilator

A. Mathematical Model of High-Altitude Ventilator

The inlet and outlet of the ventilator face the atmosphere and the airbag, respectively, as shown in Fig. 1. The atmospheric states of ventilator inlet varies with flying height of airship, and the static pressure difference between ventilator inlet and outlet changes as the operating state of the airship. Thence, the mathematical model of high-altitude ventilator contains four state variables, which are volume flow, static pressure difference, rotating speed and height, respectively. These variables are mutual coupling and have the nonlinear relationship. In order to realize the precise control of the ventilator, it is necessary to establish the mathematical model of high-altitude ventilator.

When the ventilator operates at rated speed at 0 km, the mathematical model of ventilator is the binary function about

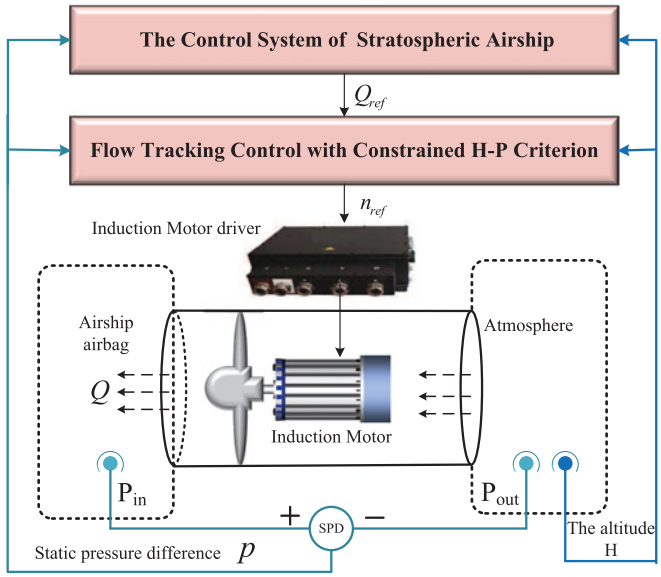

Fig. 1. High-altitude ventilator.

volume flow and static pressure difference. Based on the discrete operating points calculated by means of experimental measurement or finite-element method, the polynomial mathematical model of the ventilator is established by using the data fitting method. The polynomial mathematical model is shown as (1). The relationship between static pressure difference p_e and volume flow Q_e is shown in (1a), where the coefficients α_i are obtained by data fitting method, and the relationship between ventilator input shaft power and volume flow is shown in (1b):

$$p_e = \sum_{i=0}^{n} \alpha_i Q_e^i \tag{1a}$$

$$P_e = \sum_{j=0}^{m} \beta_j Q_e^j. \tag{1b}$$

The above equation (1) is the mathematical model of the ventilator at rated speed n_e at the altitude of 0 km. When the altitude is H, the air density ρ can be expressed as [33] follows:

$$\rho = 1.2258(1 - 0.02257H)^{4.256}\ \text{kg/m}^3 (H \le 11\,\text{km}) \tag{2a}$$

$$\rho = 1.2258 \times 1.684e^{-1.578H}\ \text{kg/m}^3 (H > 11\,\text{km}). \tag{2b}$$

The four-dimensional mathematical model of high-altitude ventilator can be established by similar principles. The similar principles are shown as (3), where Q_e, ρ_e, n_e, p_e, P_e represent the operating values of high-altitude ventilator at 0 km, and Q, ρ, n, p, P represent other operating states of high-altitude ventilator

$$Q = Q_e n/n_e = NQ_e \tag{3a}$$

$$p = p_e(n/n_e)^2(\rho/\rho_e) = N^2 p_e(\rho/\rho_e) \tag{3b}$$

$$P = P_e(n/n_e)^3(\rho/\rho_e) = N^3 P_e(\rho/\rho_e). \tag{3c}$$

Equations (1) and (2) are substituted into (3) and then (4) can be obtained, which is the four-dimensional mathematical

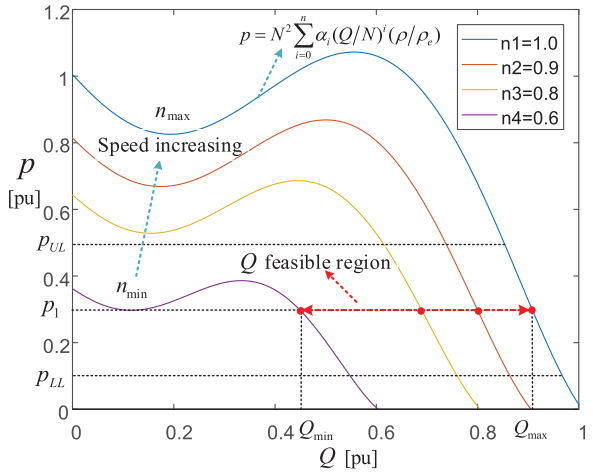

Fig. 2. Curve of static pressure difference and volume flow.

model of high-altitude ventilator. The more accurate mathematical model can be obtained by mathematical interpolation method with the more discrete operating points at different speeds and different heights. From (4), the static pressure difference is the function of the volume flow, the speed, and operating height, so is the shaft power

$$p = f(Q, n, H) = N^2 \sum_{i=0}^{n} \alpha_i (Q/N)^i (\rho/\rho_e) \tag{4a}$$

$$P = g(Q, n, H) = N^3 \sum_{j=0}^{n} \beta_j (Q/N)^j (\rho/\rho_e). \tag{4b}$$

B. Control Strategy of High-Altitude Ventilator

As shown in Fig. 1, the role of the ventilator is to output the reference volume flow of the air by adjusting the speed under the constraints of the static pressure difference and flight height. When the airship is in flight, the static pressure difference p and the height H can be obtained by the sensors. Therefore, (4a) is degenerated to the binary function about the speed and the volume flow, which is shown in Fig. 2. By adjusting the ventilator speed, the reference volume flow can be obtained. As shown in Fig. 2, the output volume flow of the ventilator is limited between $Q_{\min}$ and $Q_{\max}$. The maximum flow $Q_{\max}$ can be obtained from the maximum output power of induction motor, while the minimum flow $Q_{\min}$ can be obtained from the ventilator stable operation area. $p_{\rm LL}$ presents lower limit value of static pressure difference, and insufficient static pressure difference will cause the deformation of the airship structure. $p_{\rm UL}$ presents upper limit value of this static pressure, and excessive static pressure difference will cause the airship to expand and crack. The diagram of the flow tracking is shown in Fig. 3. First, the two-dimensional function with Q and n can be obtained when the constrains p, H are known by the sensors. Second, compute $Q_{\min}$ and $Q_{\max}$. Third, the reference speed n_{ref} can be obtained by the two-dimensional function with Q and n.

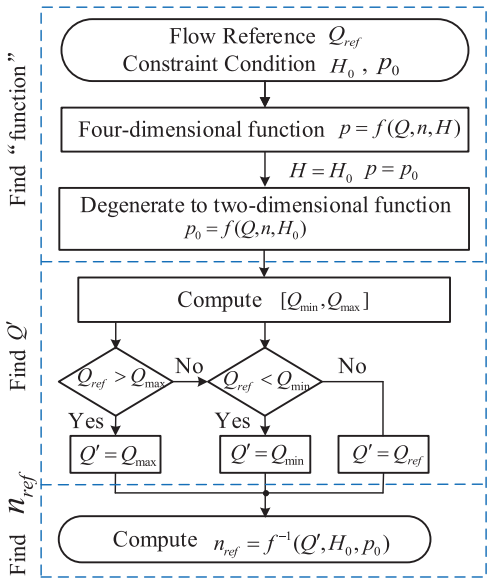

Fig. 3. Diagram of flow tracking control strategy.

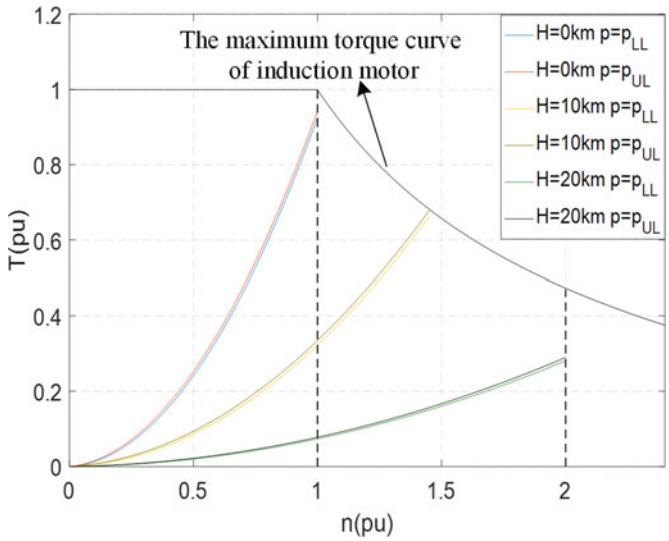

Fig. 4. *T–n* curve of high-altitude ventilator.

C. Load Characteristic of High-Altitude Ventilator

When the rated values at 0 km are defined as base values, *T–n* curve of high-altitude ventilator at different height is shown in Fig. 4. As can be seen from Fig. 4, the load torque of high-altitude ventilator is 0.32 p.u. at 10 km, and the load torque of high-altitude ventilator is only 0.28 p.u. at 20 km. It is obvious that induction motor is in the light-load condition in field-weakening mode. The traditional variable voltage variable frequency control strategy of induction motor leads to the waste of energy for the airship with energy shortage. In order to save energy, the field current and torque current of induction motor should be optimized according to the load torque of high-altitude ventilator.

III. Extended Minimum Stator Current Control of High-altitude ventilator Induction Motor

A. Mathematical Model of High-Altitude Ventilator Induction Motor

The vector mathematical model of three-phase winding induction motor at the reference frame rotating with any speed w can be described as (5)–(7). L_s, L_r, and L_m are the stator inductance, the rotor inductance, and magnetizing inductance, respectively. As shown in [34], L_m is treated as a nonlinear parameter, which is updated in every sampling period. First, L_m can be considered as the constant value for the convenience of analysis. R_s and R_r are the stator resistance and the rotor resistance, respectively. i_s^w, ψ_s^w, and v_s^w are the current vector, flux linkage vector, and voltage vector of the stator, respectively; similarly, i_r^w, ψ_r^w, and v_r^w are the current vector, flux linkage vector, and voltage vector of the rotor, respectively. The electromagnetic torque T_e can be viewed as the result of the interaction between i_s^w and ψ_r^w and P represents the pole pairs among the (9)

$$v_s^w = R_s i_s^w + \frac{d\psi_s^w}{dt} + jw\psi_s^w \tag{5}$$

$$0 = R_r i_r^w + \frac{d\psi_r^w}{dt} + j\left(w - w_r\right)\psi_r^w \tag{6}$$

$$\psi_s^w = L_s i_s^w + L_m i_r^w \tag{7}$$

$$\psi_r^w = L_m i_s^w + L_r i_r^w \tag{8}$$

$$T_e = \frac{3}{2}P\frac{L_m}{L_r}\mathrm{Im}\left\{\overline{\psi_r^w} i_s^w\right\}. \tag{9}$$

When the reference frame rotates with the angular frequency w_e of the rotor flux linkage vector, the stator current vector can be described as (10), where i_{ds}^e and i_{qs}^e are d-axis current component and q-axis current component. The q-axis component of rotor flux linkage vector ψ_{qr}^e is zero, namely, $\psi_{qr}^e = 0$. ψ_{dr}^e can be described as (11), where i_{ds}^e is field current and p is the differential operator. When i_{ds}^e is kept as the constant for a period of time ($t \geq \frac{4L_r}{R_r}$), the electromagnetic torque T_e can be written as (12), where i_{qs}^e denotes the torque current

$$i_s^e = i_{ds}^e + ji_{qs}^e \tag{10}$$

$$\psi_{dr} = \frac{L_m}{1 + p\left(L_r/R_r\right)} i_{ds} \tag{11}$$

$$T_e = \frac{3}{2}P\frac{L_m^2}{L_r} i_{ds} i_{qs} \tag{12}$$

B. Extended Minimum Stator Current Control of Induction Motor

Based on (12), i_{ds}^e and i_{qs}^e are not unique to produce the desired torque and this provides an additional freedom to coordinate i_{ds}^e and i_{qs}^e. In this paper, the additional freedom is utilized to realize the minimum stator current. The minimum stator current control strategy can enhance the induction motor efficiency and lower inverter capacity. It is the optimal problem to obtain minimum stator current with the desired torque. This optimal problem can be described as follows:

$$\min \quad I_s = \sqrt{\left(i_{ds}^e\right)^2 + \left(i_{qs}^e\right)^2} \tag{13a}$$

$$\text{s.t.} \quad \left(w_e \sigma L_s i_{qs}^e\right)^2 + \left(w_e L_s i_{ds}^e\right)^2 \leq V_{s\max}^2 \tag{13b}$$

$$\left(i_{ds}^e\right)^2 + \left(i_{qs}^e\right)^2 \leq I_{s\max}^2 \tag{13c}$$

$$\frac{3}{2}p\frac{L_m^2}{L_r} i_{ds}^e i_{qs}^e = T \tag{13d}$$

$$T \leq T_m\left(w_e\right) \tag{13e}$$

$$i_{ds}^e \leq i_{ds\_\mathrm{rate}}. \tag{13f}$$

Equation (13a) is the objective function of the constrained optimization problem. Equation (13b) is voltage constrain, which is subject to the invert voltage rating and the insulation performance of induction motor. $V_{s\max}$ is obtained by the formula $V_{s\max} = (V_d/\sqrt{3})\mu$, where μ is a factor less than 1 in order to consider the fluctuations of the bus voltage V_d. σ is leakage coefficient that is defined by $\sigma = \left(L_s L_r - L_m^2\right)/L_s L_r$. Equation (13c) is current constrain, which is subject to the thermal limit of the invert and induction motor. The desired torque T is defined by (13d). The constrain (13e) describes the maximum torque provided by induction motor, where the solution of T_m can be described as other constrain optimal problem

$$\max \quad T_m = \frac{3}{2}p\frac{L_m^2}{L_r} i_{ds}^e i_{qs}^e \tag{14a}$$

$$\text{s.t.} \quad \left(w_e \sigma L_s i_{qs}^e\right)^2 + \left(w_e L_s i_{ds}^e\right)^2 \leq V_{s\max}^2 \tag{14b}$$

$$\left(i_{ds}^e\right)^2 + \left(i_{qs}^e\right)^2 \leq I_{s\max}^2 \tag{14c}$$

$$i_{ds}^e \leq i_{ds\_\mathrm{rate}}. \tag{14d}$$

The optimal problem (13) is the constrained nonlinear programming problem, which is hard to solve with the parameters in general. However, the optimal problem (13) can be decomposed into subproblems that can be solved by the properties of system, such as the minimum stator current curve, constant torque curve, and the voltage constraint ellipse. The solution is composed of three modes, the constant torque mode, the constant power mode, and the constant voltage mode. Three modes are divided based on the synchronous electromagnetic speed w_e. The w_e range of the constant torque model is $0 < w_e \leq w_{\mathrm{base}}$, where w_{base} is described in (15). i_{ds_rate} is the rated current of induction motor. The w_e range of the constant power model is $w_{\mathrm{base}} < w_e \leq w_1$, where w_1 is described in (16). The w_e range of the constant voltage model is $w_1 < w_e$. The diagram of the optimal problem is shown in Fig. 5

$$w_{\mathrm{base}} = \frac{V_{s\max}}{\sqrt{i_{ds\_\mathrm{rate}}^2\left(L_s^2 - \sigma^2 L_s^2\right) + \left(\sigma L_s I_{s\max}\right)^2}} \tag{15}$$

$$w_1 = \left(V_{s\max}/I_{s\max}\right)\sqrt{\left(L_s^2 + \sigma^2 L_s^2\right)/\left(2L_s^4\sigma^2\right)}. \tag{16}$$

1) Constant Torque Mode ($0 < w_e \leq w_{\mathrm{base}}$): Because excessive field current can make magnetic circuit saturation of

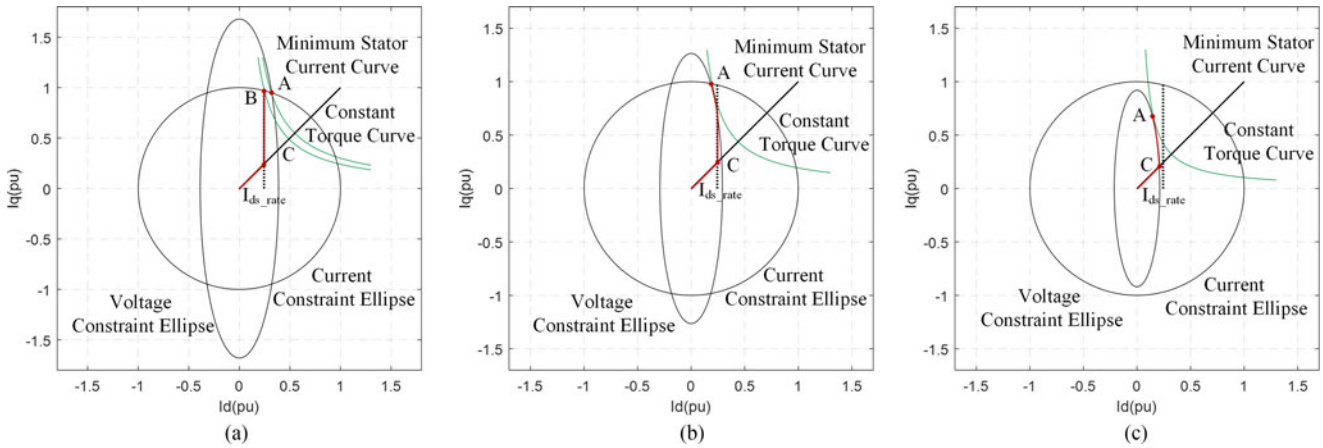

Fig. 5. Three modes of induction motor with extended minimum stator current operation. (a) Constant torque model. (b) Constant power model. (c) Constant voltage model.

induction rotor, the d-axis current is limited to i_{ds_rate}. The maximum torque $T_{\max}$ is described as (17a). If the desired torque T exceeds $T_{\max}$, it is supposed that the drive system can provide the largest available torque $T_{\max}$

$$T_{\max} = \frac{3}{2} p \frac{L_m^2}{L_r} i_{ds}^e \sqrt{i_{s\max}^2 - \left(i_{ds}^e\right)^2} \tag{17a}$$

$$i_{ds}^e = i_{ds\_\mathrm{rate}}. \tag{17b}$$

If $T < T_{\max}$, the d-axis current i_{ds}^e and q-axis current i_{qs}^e are obtained by the minimum stator current curve, which are described as (18a) and (18b). The diagram of the optimal problem in the constant torque model is shown in Fig. 5

$$i_{ds}^e = \min\left(\sqrt{2TL_r/\left(3pL_m^2\right)}, i_{ds\_\mathrm{rate}}\right) \tag{18a}$$

$$i_{qs}^e = 2TL_r/\left(3pL_m^2 i_{ds}^e\right). \tag{18b}$$

2) Constant Power Mode ($w_{\mathrm{base}} < w_e \le w_1$): From the current plane of Fig. 5, it is known that the maximum torque is obtained when the stator current is located in the intersection of the voltage elliptical and current elliptical. The maximum torque $T_{\max}$, d-axis current i_{ds}^e, and q-axis current i_{qs}^e are, respectively, given as follows:

$$T_{\max}\left(w_e\right) = 3pL_m^2 i_{ds}^e i_{qs}^e/(2L_r) \tag{19a}$$

$$i_{ds}^e = \frac{\sqrt{\left(V_{s\max}/w_e\right)^2 - \left(\sigma L_s I_{s\max}\right)^2}}{\sqrt{L_s^2 - \left(\sigma L_s\right)^2}} \tag{19b}$$

$$i_{qs}^e = \sqrt{I_{s\max}^2 - \left(i_{ds}^e\right)^2}. \tag{19c}$$

The $i_{ds\_pi}^e$ denotes the corresponding d-axis current of intersection point of the voltage elliptical and constant torque curve. The optimal d-axis current is expressed in (20), where T_c represents the torque at the point C in Fig. 5

$$i_{ds}^e = \begin{cases} \min\left(\sqrt{\frac{2TL_r}{3pL_m^2}}, i_{ds\_\mathrm{rate}}\right), & \text{for } 0 \le T < T_c \\ \min\left(i_{ds\_pi}^e, i_{ds\_\mathrm{rate}}\right), & \text{for } T_c \le T < T_{\max} \end{cases} \tag{20a}$$

$$i_{qs}^e = 2TL_r/\left(3pL_m^2 i_{ds}^e\right). \tag{20b}$$

3) Constant Voltage Mode ($w_1 < w_e$): The $T_{\max}$, i_{ds}^e, and i_{qs}^e are, respectively, given as follows:

$$T_{\max}\left(w_e\right) = 3pL_m^2 i_{ds}^e i_{qs}^e/(2L_r) \tag{21a}$$

$$i_{ds}^e = V_{s\max}/\left(\sqrt{2}w_e L_s\right) \tag{21b}$$

$$i_{qs}^e = V_{s\max}/\left(\sqrt{2}w_e \sigma L_s\right). \tag{21c}$$

The optimal d-axis current can be expressed as (22), where the meanings of variables are as same as ones of the constant power mode

$$i_{ds}^e = \begin{cases} \min\left(\sqrt{\frac{2TL_r}{3pL_m^2}}, i_{ds\_\mathrm{rate}}\right), & \text{for } 0 \le T < T_c \\ \min\left(i_{ds\_pi}^e, i_{ds\_\mathrm{rate}}\right), & \text{for } T_c \le T < T_{\max} \end{cases} \tag{22a}$$

$$i_{qs}^e = 2TL_r/\left(3pL_m^2 i_{ds}^e\right). \tag{22b}$$

The diagram of EMSCO is shown in Fig. 6. The first step is to identify the operation mode. The second step is to compute the maximum torque $T_{\max}$. The third step is to obtain the optimal stator current references.

IV. Optimal Duty Cycle Model Predictive Current Control

Based on the mathematical model of induction motor in Section III, the stator current can be described as (23) in the

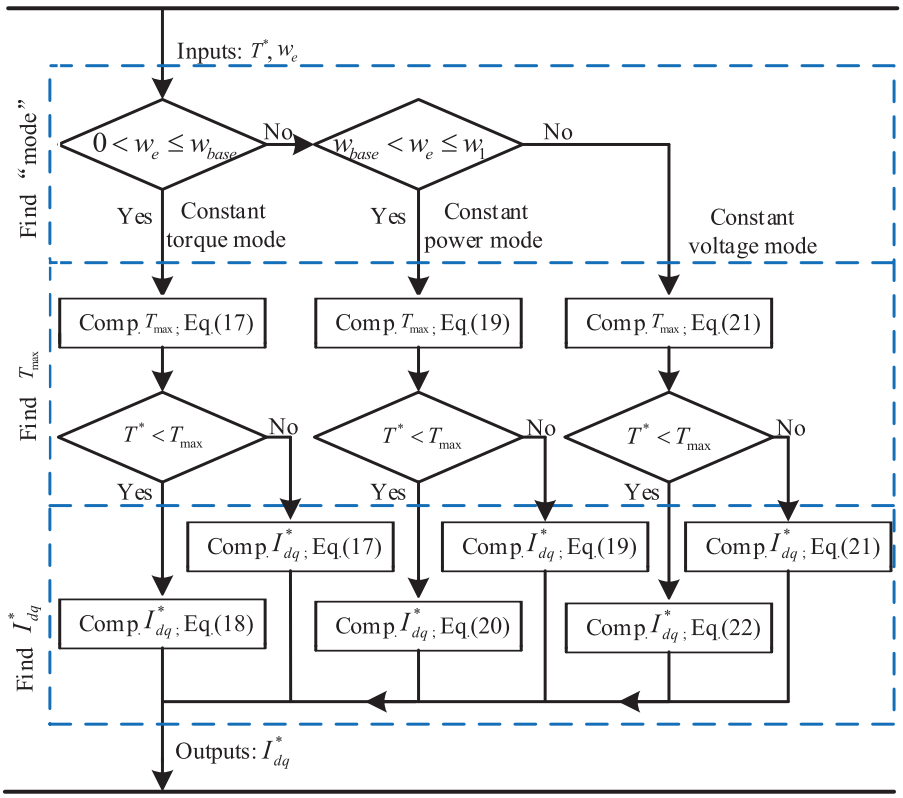

Fig. 6. Diagram of extended minimum stator current operation.

stator reference frame [35]

$$i_s + \tau_\sigma \frac{di_s}{dt} = \frac{k_r}{R_\sigma}\left(\frac{1}{\tau_r} - jw\right)\psi_r + \frac{v_s}{R_\sigma}. \tag{23}$$

In order to obtain the discrete model, the forward Euler discretization is adopted

$$y_{k+1} = y_k + T_s f\left(x_k, y_k\right) \tag{24}$$

where T_s is the sampling time of the control system. Then, the discrete equation of stator current can be described as (25). Different voltage vectors at k sampling time are used to predict stator currents at $k+1$ sampling time. The optimal voltage vector will be selected, which makes the cost function minimum

$$i_s(k+1) = \left(1 - \frac{T_s}{\tau_\sigma}\right) i_s(k) + \frac{T_s}{\tau_\sigma}\frac{k_r}{R_\sigma} \cdot \left(\frac{1}{\tau_r} - jw\right)\psi_r(k) + \frac{T_s}{\tau_\sigma R_\sigma} v_s(k). \tag{25}$$

The discrete equation of stator current (25) can also be rewritten as (26a), where k_1 and k_2 are, respectively, (26c) and (26b)

$$i_s(k+1) = k_1 + k_2 v_s\,(k) \tag{26a}$$

$$k_2 = \frac{T_s}{\tau_\sigma R_\sigma} \tag{26b}$$

$$k_1 = \left(1 - \frac{T_s}{\tau_\sigma}\right) i_s(k) + \frac{T_s}{\tau_\sigma}\frac{k_r}{R_\sigma} \cdot \left(\frac{1}{\tau_r} - jw\right)\psi_r(k). \tag{26c}$$

Assume the stator current reference at $k+1$ sampling time is $i_s^*(k+1)$. The deadbeat voltage vector $v_s^*(k)$ is defined as the voltage vector, which makes the stator current reach the reference value $i_s^*(k+1)$ at $k+1$ sampling time. Thence, the stator current reference $i_s^*(k+1)$ and the deadbeat voltage vector $v_s^*(k)$ satisfy

$$i_s^*(k+1) = k_1 + k_2 v_s^*\,(k)\,. \tag{27}$$

In this paper, in order to reduce the stator current ripple, two voltage vectors at one sampling period will be utilized. Assuming that two selected voltage vectors are denoted as u_x and u_y. The duty ratios of u_x and u_y are denoted as α_x and α_y. The equation $v_s(k) = \alpha_x u_x + \alpha_y u_y$ can be obtained. By (26a) and (27), the cost function can be expressed as

$$\begin{aligned} g_{xy} &= \left|i_s^*(k+1) - i_s(k+1)\right| \\ &= \left|k_1 + k_2 v_s^*\,(k) - \left[k_1 + k_2 v_s\,(k)\right]\right| \\ &= k_2\left|v_s^*(k) - \left(\alpha_x u_x + \alpha_y u_y\right)\right|. \end{aligned} \tag{28}$$

In view of u_x and u_y, the solution of α_x and α_y can be formalized in the form of an optimization problem as follows:

$$\min \quad g_{xy}(\alpha_x, \alpha_y) \tag{29a}$$

$$\text{s.t.} \quad \alpha_x + \alpha_y = 1 \tag{29b}$$

$$0 \le \alpha_x \le 1. \tag{29c}$$

Assume u_x is not equal to u_y. By solving the optimization problem (29), the duty ratio α_x of u_x can be expressed as (30a).

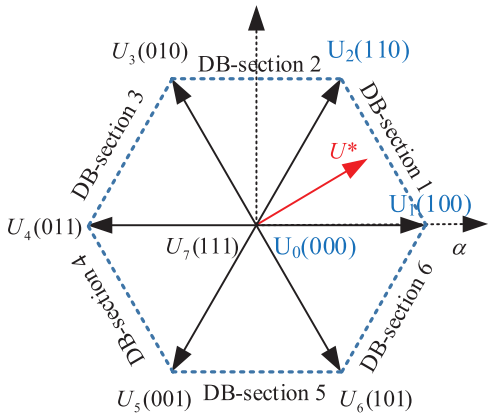

Fig. 7. Vectors of 2-level voltage source inverter.

TABLE I
SELECTED VECTORS OF ODC-MPCC BY DEADBEAT VECTOR

Angle-DB	DB-sector	Selected vectors	Selected pairs
$[0, \pi/3]$	1	U_0, U_1, U_2	U_{01}, U_{02}, U_{12}
$(\pi/3, 2\pi/3]$	2	U_0, U_2, U_3	U_{02}, U_{03}, U_{23}
$(2\pi/3, \pi]$	3	U_0, U_3, U_4	U_{03}, U_{04}, U_{34}
$(\pi, 4\pi/3]$	4	U_0, U_4, U_5	U_{04}, U_{05}, U_{45}
$(4\pi/3, 5\pi/3]$	5	U_0, U_5, U_6	U_{05}, U_{06}, U_{56}
$(5\pi/3, 2\pi]$	6	U_0, U_6, U_1	U_{06}, U_{01}, U_{61}

The cost function (28) can be expressed as (30b)

$$\alpha_x = [(v_s^*(k) - u_y)(u_x - u_y)]/|u_x - u_y|^2 \tag{30a}$$

$$g_{xy} = k_2 \left| v_s^*(k) - [\alpha_x u_x + (1 - \alpha_x) u_y] \right|. \tag{30b}$$

For the two-lever voltage source inverter, eight voltage vectors can be produced, six active vectors and two zero vectors, respectively. These voltage vectors can generate 21 pairs of voltage vectors. If the cost function g_{xy} of every pair of voltage vectors is computed in one sampling period, it will produce much computation burden. In this paper, three voltage vectors are first selected by the deadbeat voltage vector, and then the selected three vectors will only produce three pairs of vectors. For example, if the deadbeat voltage vector is located in the DB-section 1, the voltage vectors U_0, U_1, U_2 will be selected as shown in Fig. 7. These three vectors will produce three pairs of vectors U_{01}, U_{02}, U_{12} as shown in Table I, where U_{01} represents one pair of vectors, U_0 and U_1. The cost functions of three pairs will be computed according to (30). The optimal pair will be selected, whose cost function is minimum.

The implementation of the proposed ODC-MPCC will be divided into five steps as shown in Fig. 8. In Step 1, obtain $i_s^*(k+1)$, $i_s(k)$, and $\hat{\psi}_r(k)$. In Step 2, compute the deadbeat voltage vector based on (26) and (27). In Step 3, select three pairs of voltage vectors based on Table I. In Step 4, compute the cost function of every pair, respectively. In Step 5, select the optimal pair of vectors, which can make the cost function minimum. Then, apply the optimal pair of vectors at $k+1$ sampling time.

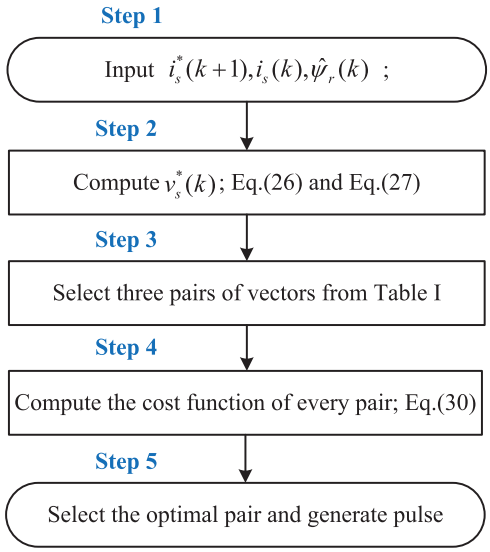

Fig. 8. Diagram of ODC-MPCC.

For example, the optimal pair of vectors are U_0 and U_1, and the duty ratio of U_0 is α_0. At $k+1$ time, the voltage vector U_0 will be applied and lasts for $\alpha_0 T_s$, then the voltage vector U_1 will be applied until the $k+2$ time.

Fig. 9 illustrates the block diagram of ODC-MPCC of induction motor with EMSCO, which mainly consists of two parts, extended minimum stator current operation and ODC-MPCC. The diagrams of two parts are, respectively, shown in Figs. 6 and 8. The speed reference can be obtained from the flow tracking control strategy shown in Fig. 3. In order to consider the nonlinearity of magnetizing inductance L_m [34], $L_m(i_{ds}^e)$ can be obtained by experimental method. At the end of each sampling cycle, L_m will be updated by the look-up table method.

V. SIMULATION AND EXPERIMENT

A. Simulation Analysis

The proposed ODC-MPCC of high-altitude ventilator induction motor with EMSCO is tested by simulation with MATLAB/Simulink, and is compared with traditional control strategy of induction motor. For traditional control strategy of induction motor, the field current is set as (17b) at constant torque mode, (19b) at constant power mode, and (21b) at constant voltage mode. The parameters of induction motor are listed in Table II. The sampling period is set as 0.1 ms. $I_{s\max}$ is set to the rated current of induction motor. In order to compare two algorithms, the same anti-windup proportional–integral controller for the speed loop is applied [36].

First, the speed reference is set as 1 p.u. at 0 s, and 2 p.u. at 0.3 s. The response of speed, torque, stator current, and *dq*-axial current is shown in Fig. 10. At the stage of acceleration, owing to the speed reference is too lager so that the speed controller saturates, and outputs the maximum torque reference. The part of EMSCO produces the rotor flux linkage reference and the *d*-axial current reference based on the torque reference. The rotor

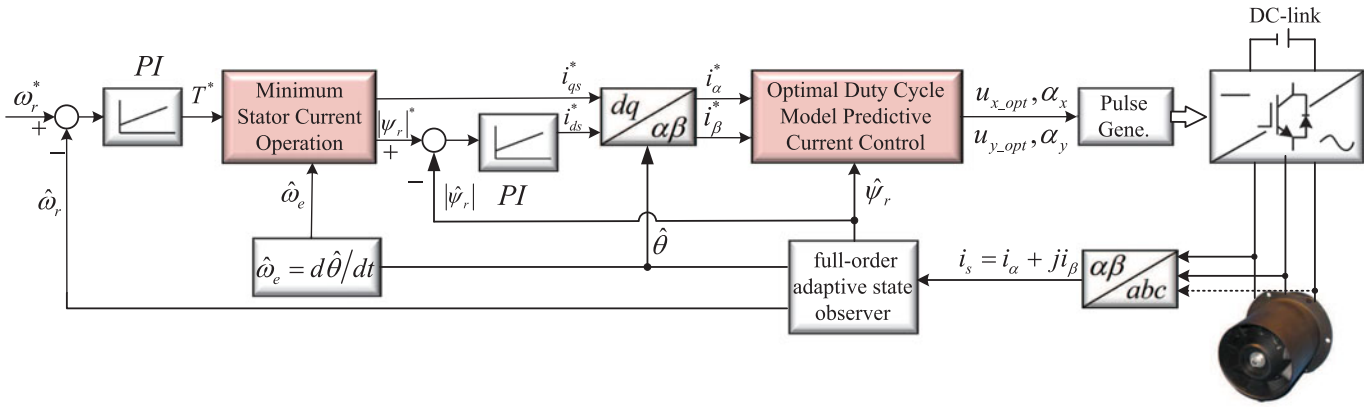

Fig. 9. Block diagram of ODC-MPCC of induction motor with EMSCO.

TABLE II
PARAMETERS OF INDUCTION MOTOR

Rated power	P_N	3.6 kW
Rated voltage	U_N	150 V
Rated current	I_N	16.8 A
Rated frequency	f_N	150 Hz
Rated torque	T_N	4.0 N · m
Number of pole pairs	N_p	1
Rated field current	I_{ds_rate}	5.8 A

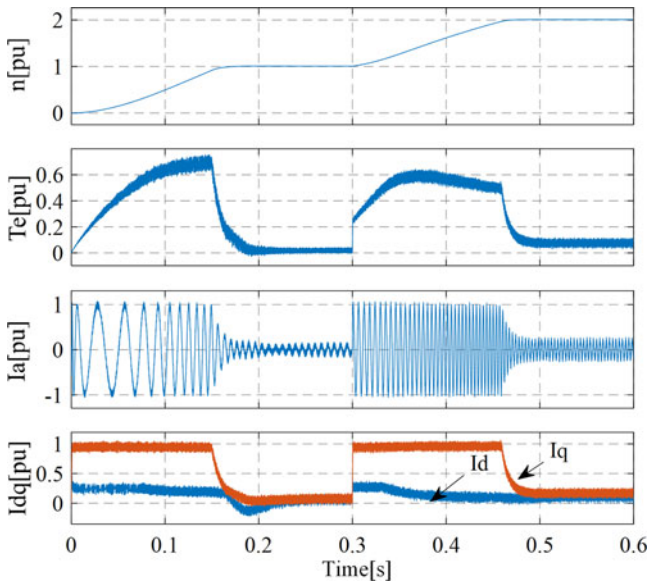

Fig. 10. Dynamic response of induction motor by simulation.

flux linkage is controlled by the *d*-axial current based on (11), which is the first-order inertia system. Because the rotor flux linkage is controlled by the *d*-axial current at a delay of rotor time constant, the torque cannot immediately reach its reference and has the response process as shown in Fig. 10. When the speed of induction motor rises above the base value, because of the voltage ellipse limit, the maximum output torque decreases as the speed increases. When the speed reaches its reference, the optimal *dq*-axial current based on the load torque is produced by the part of EMSCO. From Fig. 10, induction motor operates in constant torque mode at 0.25 s, and in constant power mode at 0.55 s. The response of dq-axial is quickly because MPCC directly chooses the optimal pair of voltage vectors.

To verify the effectiveness of EMSCO at steady stage, different load torques are set at different speed references. The cases are as follows:

1) $w = 1.0$ p.u. with $T = 0.05, 0.2, 0.5, 0.75, 1.0$ p.u.;
2) $w = 2.0$ p.u. with $T = 0.05, 0.2, 0.5$ p.u.

are evaluated, and the simulation results are shown in Fig. 11. The detailed data are listed in Tables III and IV. The *d*-axial current reference of traditional control strategy below rated speed is the rated field current, while that of the proposed EMSCO algorithm varies with the load torque. The proposed EMSCO algorithm can reduce the stator current at light-load state. At the speed of 2.0 p.u., owing to the voltage ellipse limit, the maximum output torque decreases to 0.5 p.u., while the EMSCO algorithm can also minimize the stator current at light-load state.

In order to evaluate the influence of variable magnetizing inductance on the computation of i_{ds}^* and i_{qs}^*, $\hat{i}_{ds}^*$ and $\hat{i}_{qs}^*$ are obtained by EMSCO with $\hat{L}_m$ and L_m, where $\hat{L}_m$ is set as $\hat{L}_m = 1.5L_m$. From Fig. 12, as the speed increases, the influence of variable magnetizing inductance on i_{ds}^* and i_{qs}^* is reduced.

B. Experiment Analysis

The proposed ODC-MPCC of high-altitude ventilator induction motor with EMSCO is experimentally tested on two-lever inverter-fed induction motor platform, which is illustrated in Fig. 13. The high-altitude ventilator is placed in low pressure chamber that can simulate the low-pressure state at high altitude. The parameters of induction motor is listed in Table II, and the axial ventilator is driven by induction motor. The platform adopts two-lever voltage source inverter to drive induction motor, and the dc-bus voltage is provided by the dc power supply cabinet. A 32-bit floating point digital signal processing

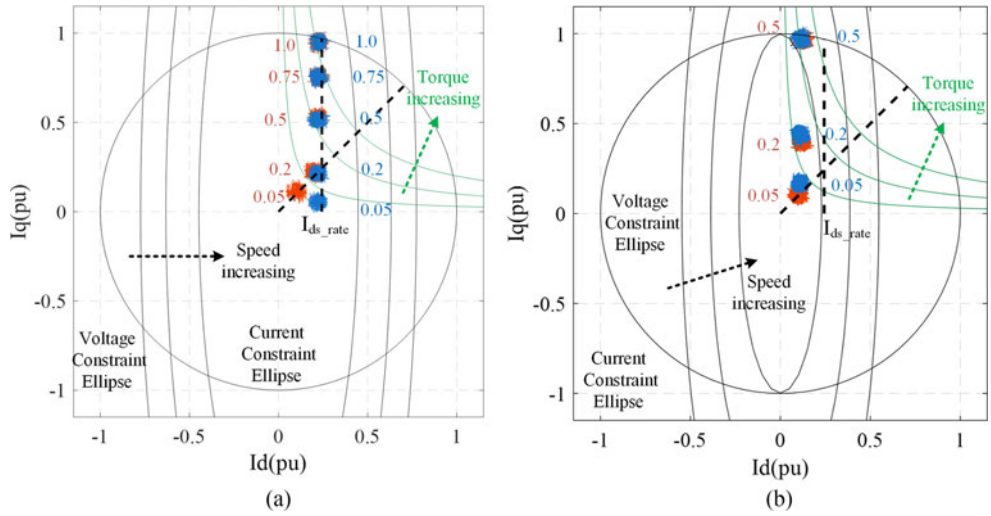

Fig. 11. Steady-state points by simulation. (a) $w = 1.0$ p.u. (b) $w = 2.0$ p.u.

TABLE III
STEADY-STATE OPERATION WITH $w = 1.0$ P.U. BY SIMULATION

T_L [p.u.]	0.05	0.20	0.50	0.75	1.00
Trad_I_d [p.u.]	0.2225	0.2219	0.2226	0.2234	0.2246
EMSCO_I_d [p.u.]	0.1039	0.2024	0.2236	0.2235	0.2242
Trad_I_q [p.u.]	0.0547	0.2137	0.5152	0.7547	0.9497
EMSCO_I_q [p.u.]	0.1150	0.2240	0.5292	0.7551	0.9486
Trad_I_s [p.u.]	0.2291	0.3080	0.5612	0.7870	0.9759
EMSCO_I_s [p.u.]	0.1550	0.3020	0.5745	0.7875	0.9747

TABLE IV
STEADY-STATE OPERATION WITH $w = 2.0$ P.U. BY SIMULATION

T_L [p.u.]	0.05	0.20	0.50
Trad_I_d [p.u.]	0.1076	0.1099	0.1151
EMSCO_I_d [p.u.]	0.1001	0.1176	0.1263
Trad_I_q [p.u.]	0.1697	0.4394	0.9738
EMSCO_I_q [p.u.]	0.1051	0.3998	0.9702
Trad_I_s [p.u.]	0.2010	0.4529	0.9805
EMSCO_I_s [p.u.]	0.1451	0.4168	0.9784

(DSP) TMS320F28335 serves as the control core to accomplish the proposed algorithm. The stator current of induction motor is transferred to the DSP by A/D converter module. The speed command is transferred to the DSP by serial interface. All variables are displayed on the digital oscilloscope by the D/A converter module. The data are further transferred to PC for plotting with MATLAB. In the experiment, the sampling frequency of the control system is 10 kHz.

First, the high-altitude ventilator is put into low-pressure chamber, and then the pressure of low-pressure chamber is reduced to 5530 Pa, which is the atmospheric pressure at 20 km. Then, the speed reference is set as 1 p.u. at 0 s, and 2 p.u. at 0.3 s. The response of variables of induction motor is illustrated in Fig. 14. In the acceleration stage, due to excellent dynamic performance of ODC-MPCC, d-axis current quickly reaches its reference value, while the torque rises up slowly at a delay of rotor time constant. At the steady stage, the minimum stator current is obtained to meet the torque requirement.

In order to verify the steady performance of the proposed algorithm, the different pressures of low-pressure chamber will be set at different speeds, which are shown as follows:

1) $w = 1.0$ p.u. with $p_a = 0.05$, 0.2, 0.5, 0.75, 1.0 p.u.;
2) $w = 2.0$ p.u. with $p_a = 0.05$, 0.075, 0.12 p.u.

The base value of pressure is the standard atmospheric pressure 101 325.0 p_a.

Because the ventilator load torque is proportional to the density of the air based on similar principles of ventilator, induction motor can operate in light-load condition by reducing the pressure of low-pressure chamber. The experiments results are shown in Fig. 15. Compared with the traditional method, the proposed algorithm can optimize stator current as shown in Tables V and VI. When the pressure is 0.05 p.u. at $w = 1.0$ p.u., the traditional method needs 0.2633 p.u. I_s to meet the torque requirement, while the proposed algorithm only needs 0.1856 p.u. I_s, which reduces by 29.51%. The reduced I_s makes copper loss lower, and the reduced I_d makes the iron loss lower. So, the proposed EMSCO can obtain smaller losses and lower temperature of induction motor.

The third test is to compare the current ripple and computation burden of the proposed ODC-MPCC and the traditional MPCC (TMPCC). The time consumption of ODC-MPCC and TMPCC is tested by TMS320F28335. In one sampling period, the computation time of TMPCC is 54 μs, while that of ODC-MPCC is 32 μs. The computation of ODC-MPCC is 40.7% less than that of TMPCC. In order to compare the current ripple of two methods, I_{ds_ripple} and I_{qs_ripple} are defined as (31) and (32), respectively, where I_{ds_i} and I_{qs_i} are the instant values of d-axial current and q-axial current, respectively, and I_{ds_av} and

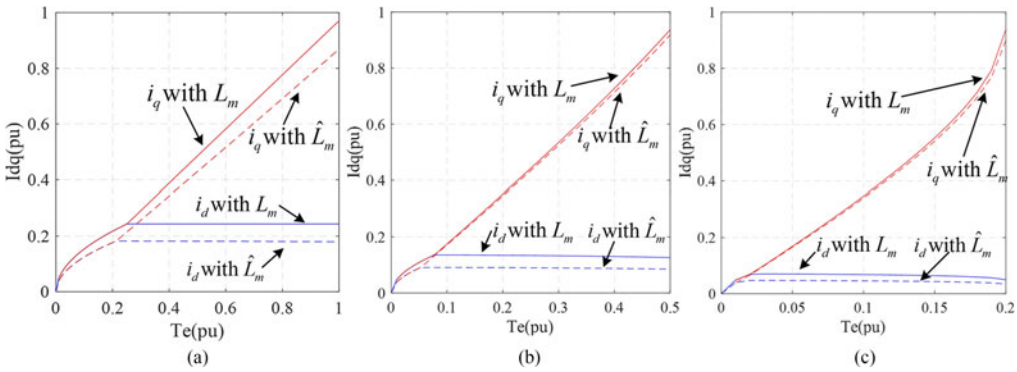

Fig. 12. Influence of variable magnetizing inductance on current reference computation. (a) Constant torque mode. (b) Constant power mode. (c) Constant voltage mode.

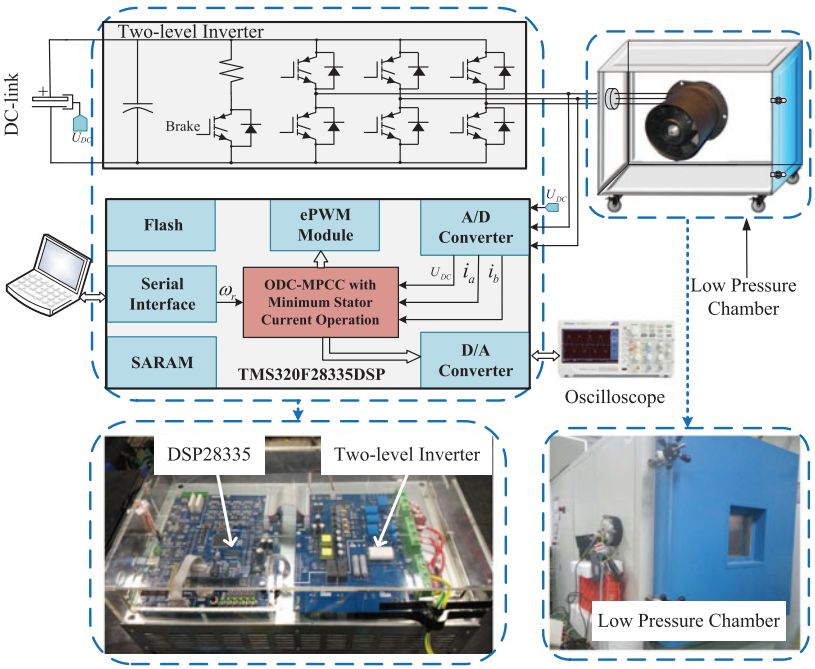

Fig. 13. Block diagram of the experimental setup.

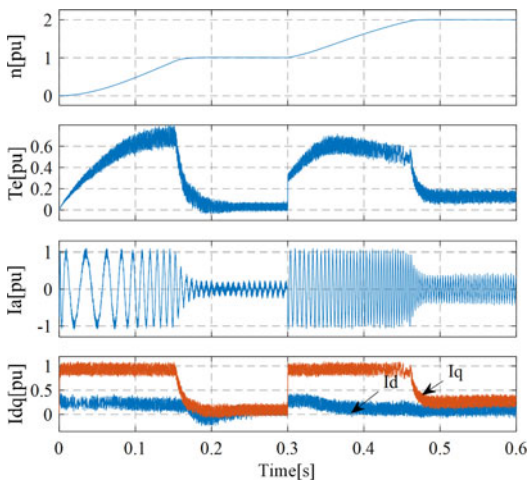

Fig. 14. Dynamic response of induction motor by experiment.

I_{ds_av} are the average values

$$I_{ds\_\text{ripple}} = \sqrt{(1/n)\sum_{i=1}^{n}(I_{d\_i} - I_{d\_av})^2} \tag{31}$$

$$I_{qs\_\text{ripple}} = \sqrt{(1/n)\sum_{i=1}^{n}(I_{q\_i} - I_{q\_av})^2}. \tag{32}$$

By the current ripple analysis of the experiment at $w = 1.0$ p.u. with T=1.0 p.u., the detail quantitative results are as shown in Table VII. According to Table VII, I_{ds_ripple} of ODC-MPCC is 1.3079, which is 47.21% less than that of TMPCC. I_{qs_ripple} of ODC-MPCC is 1.5189, which is less than that of TMPCC is 2.8144. I_{s_ripple} of ODC-MPCC is 45.92% less than that of TMPCC. The proposed ODC-MPCC has better steady-state performance than TMPCC. Because the ODC-MPCC algorithm

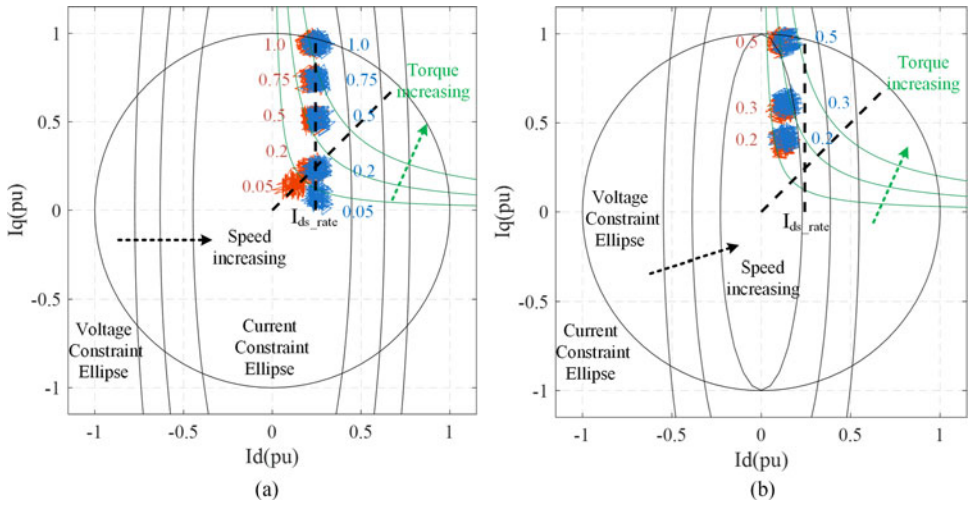

Fig. 15. Steady-state operation by experiment. (a) $w = 1.0$ p.u. (b) $w = 2.0$ p.u.

TABLE V
STEADY-STATE OPERATION WITH $w = 1.0$ P.U. BY EXPERIMENT

Pressure[p.u.]	0.05	0.20	0.50	0.75	1.00
Trad_I_d [p.u.]	0.2513	0.2538	0.2537	0.2536	0.2524
EMSCO_I_d [p.u.]	0.1217	0.2176	0.2237	0.2238	0.2224
Trad_I_q [p.u.]	0.0784	0.2300	0.5152	0.7405	0.9423
EMSCO_I_q [p.u.]	0.1402	0.2276	0.5036	0.7365	0.9322
Trad_I_s [p.u.]	0.2633	0.3426	0.5743	0.7828	0.9755
EMSCO_I_s [p.u.]	0.1856	0.3149	0.5617	0.8648	0.9682

TABLE VI
STEADY-STATE OPERATION WITH $w = 2.0$ P.U. BY EXPERIMENT

Pressure[p.u.]	0.05	0.075	0.12
Trad_I_d [p.u.]	0.1380	0.1413	0.1454
EMSCO_I_d [p.u.]	0.1195	0.1182	0.1154
Trad_I_q [p.u.]	0.4151	0.6120	0.9584
EMSCO_I_q [p.u.]	0.3874	0.5786	0.9362
Trad_I_s [p.u.]	0.4374	0.6281	0.9694
EMSCO_I_s [p.u.]	0.4054	0.5905	0.9654

TABLE VII
COMPARISON OF STEADY-STATE PERFORMANCE WITH EXPERIMENT

	TMPCC	ODC-MPCC
I_{d_ripple} [A]	2.4776	1.3079
I_{q_ripple} [A]	2.8144	1.5189
I_{s_ripple} [A]	2.7861	1.5066

adopts two voltage vectors with optimal duty ratio to track the current reference, while TMPCC uses only one voltage vector in one sampling period.

VI. CONCLUSION

In this paper, in view of the load features of high-altitude ventilator, ODC-MPCC of induction motor with EMSCO has been proposed and verified by simulation and experiment. First, the speed reference is obtained from flow tracking control strategy. Second, the field current reference and torque current reference are computed by the algorithm of EMSCO. Finally, ODC-MPCC is put forward to track the stator current. The results shows that the EMSCO algorithm can ensure the operation with minimum stator current magnitude when the load torque is small at any speed. Compared with TMPCC, the ODC-MPCC algorithm not only ensures fast response of stator current reference, but also reduces current ripple and computation burden. However, it will be the topic for future work to improve the robustness of the algorithm to the parameters of induction motor.

REFERENCES

[1] D. Zhao, D. X. Liu, K. W. Sun, G. Q. Tao, M. Zhu, and Z. Wu, "Research status, technical difficulties and development trend of stratospheric airship," *Acta Aeronautica Astron. Sin.*, vol. 37, pp. 45–56, Jan. 2016.
[2] M. C. Xiao, X. Chen, C. T. Li, and Y. Yang, "A method for altitude control of stratospheric airships," *Electron. Opt. Control*, vol. 21, pp. 86–89, Jun. 2014.
[3] X. J. Chen, H. Qi, X. P. Wang, and L. Zhou, "Modeling and simulation of pressure control for stratospheric platform airship," in *Proc. 2006 6th World Congr. Intell. Control Autom.*, Dalian, China, Jun. 2006, pp. 6208–6212.
[4] J. H. Hou, S. L. Wang, L. S. An, and H. Y. Hu, "Experimental study on flow measurement of fan based on parameter mapping," *Proc. Chin. Soc. Elect. Eng.*, vol. 23, pp. 209–214, Oct. 2003.
[5] K. Kiriakidis, A. Tzes, A. Grivas, and P.-Y. Peng, "Modeling, plant uncertainties, and fuzzy logic sliding control of gaseous systems," *IEEE Trans. Control Syst. Technol.*, vol. 7, no. 1, pp. 42–55, Jan. 1999.
[6] G. Gu, A. Sparks, and S. S. Banda, "An overview of rotating stall and surge control for axial flow compressors," *IEEE Trans. Control Syst. Technol.*, vol. 7, no. 6, pp. 639–647, Nov. 1999.
[7] F. Yao and H. Sun, "Optimal control in constant-speed fan stations," in *Proc. 2011 6th IEEE Joint Int. Inf. Technol. Artif. Intell. Conf.*, Chongqing, China, Aug. 2011, pp. 87–89.
[8] R. S. Shehata, H. A. Abdullah, and F. F. Areed, "Variable structure surge control for constant speed centrifugal compressors," *Control Eng. Pract.*, vol. 17, pp. 815–833, Feb. 2009.

[9] F. J. T. E. Ferreira, J. A. C. Fong, and A. T. de Almeida, "Ecoanalysis of variable-speed drives for flow regulation in pumping systems," *IEEE Trans. Ind. Electron.*, vol. 58, no. 6, pp. 2117–2125, Jun. 2011.
[10] P. Y. Lin and Y. S. Lai, "Novel voltage trajectory control for field-weakening operation of induction motor drives," *IEEE Trans. Ind. Appl.*, vol. 47, no. 1, pp. 122–127, Jan. 2011.
[11] Y. Liu, J. Zhao, R. Wang, and C. Huang, "Performance improvement of induction motor current controllers in field-weakening region for electric vehicles," *IEEE Trans. Power Electron.*, vol. 28, no. 5, pp. 2468–2482, May 2013.
[12] M. Mengoni, L. Zarri, A. Tani, G. Serra, and D. Casadei, "Stator flux vector control of induction motor drive in the field weakening region," *IEEE Trans. Power Electron.*, vol. 23, no. 2, pp. 941–949, Mar. 2008.
[13] S. K. Sahoo and T. Bhattacharya, "Field weakening strategy for a vector-controlled induction motor drive near the six-step mode of operation," *IEEE Trans. Power Electron.*, vol. 31, no. 4, pp. 3043–3051, Apr. 2016.
[14] B. Wang, Y. Zhao, Y. Yu, G. Wang, D. Xu, and Z. Dong, "Speed-sensorless induction machine control in the field-weakening region using discrete speed-adaptive full-order observer," *IEEE Trans. Power Electron.*, vol. 31, no. 8, pp. 5759–5773, Aug. 2016.
[15] G. D. Marques and M. F. Iacchetti, "Field-weakening control for efficiency optimization in a DFIG connected to a dc-link," *IEEE Trans. Ind. Electron.*, vol. 63, no. 6, pp. 3409–3419, Jun. 2016.
[16] D. Stojan, D. Drevensek, Z. Plantic, B. Grcar, and G. Stumberger, "Novel field-weakening control scheme for permanent-magnet synchronous machines based on voltage angle control," *IEEE Trans. Ind. Appl.*, vol. 48, no. 6, pp. 2390–2401, Nov. 2012.
[17] M. Mengoni, L. Zarri, A. Tani, G. Serra, and D. Casadei, "A comparison of four robust control schemes for field-weakening operation of induction motors," *IEEE Trans. Power Electron.*, vol. 27, no. 1, pp. 307–320, Jan. 2012.
[18] M. Preindl and S. Bolognani, "Optimal state reference computation with constrained MTPA criterion for pm motor drives," *IEEE Trans. Power Electron.*, vol. 30, no. 8, pp. 4524–4535, Aug. 2015.
[19] S. Vazquez, J. Rodriguez, M. Rivera, L. G. Franquelo, and M. Norambuena, "Model predictive control for power converters and drives: Advances and trends," *IEEE Trans. Ind. Electron.*, vol. 64, no. 2, pp. 935–947, Feb. 2017.
[20] S. Kouro, M. A. Perez, J. Rodriguez, A. M. Llor, and H. A. Young, "Model predictive control: MPC's role in the evolution of power electronics," *IEEE Ind. Electron. Mag.*, vol. 9, no. 4, pp. 8–21, Dec. 2015.
[21] C. S. Lim, E. Levi, M. Jones, N. A. Rahim, and W. P. Hew, "A comparative study of synchronous current control schemes based on FCS-MPC and PI-PWM for a two-motor three-phase drive," *IEEE Trans. Ind. Electron.*, vol. 61, no. 8, pp. 3867–3878, Aug. 2014.
[22] J. Rodriguez *et al.*, "State of the art of finite control set model predictive control in power electronics," *IEEE Trans. Ind. Informat.*, vol. 9, no. 2, pp. 1003–1016, May 2013.
[23] P. Cortes, M. P. Kazmierkowski, R. M. Kennel, D. E. Quevedo, and J. Rodriguez, "Predictive control in power electronics and drives," *IEEE Trans. Ind. Electron.*, vol. 55, no. 12, pp. 4312–4324, Dec. 2008.
[24] S. Vazquez *et al.*, "Model predictive control for single-phase NPC converters based on optimal switching sequences," *IEEE Trans. Ind. Electron.*, vol. 63, no. 12, pp. 7533–7541, Dec. 2016.
[25] Y. Wang *et al.*, "Deadbeat model-predictive torque control with discrete space-vector modulation for PMSM drives," *IEEE Trans. Ind. Electron.*, vol. 64, no. 5, pp. 3537–3547, May 2017.
[26] M. Habibullah, D. D. C. Lu, D. Xiao, and M. F. Rahman, "A simplified finite-state predictive direct torque control for induction motor drive," *IEEE Trans. Ind. Electron.*, vol. 63, no. 6, pp. 3964–3975, Jun. 2016.
[27] J. Rodriguez *et al.*, "Predictive current control of a voltage source inverter," *IEEE Trans. Ind. Electron.*, vol. 54, no. 1, pp. 495–503, Feb. 2007.
[28] C. A. Rojas, J. R. Rodriguez, S. Kouro, and F. Villarroel, "Multiobjective fuzzy-decision-making predictive torque control for an induction motor drive," *IEEE Trans. Power Electron.*, vol. 32, no. 8, pp. 6245–6260, Aug. 2017.
[29] W. Xie *et al.*, "Finite-control-set model predictive torque control with a deadbeat solution for PMSM drives," *IEEE Trans. Ind. Electron.*, vol. 62, no. 9, pp. 5402–5410, Sep. 2015.
[30] Z. Song, Y. Tian, W. Chen, Z. Zou, and Z. Chen, "Predictive duty cycle control of three-phase active-front-end rectifiers," *IEEE Trans. Power Electron.*, vol. 31, no. 1, pp. 698–710, Jan. 2016.
[31] Y. Zhang and J. Zhu, "A novel duty cycle control strategy to reduce both torque and flux ripples for DTC of permanent magnet synchronous motor drives with switching frequency reduction," *IEEE Trans. Power Electron.*, vol. 26, no. 10, pp. 3055–3067, Oct. 2011.
[32] Y. Zhang and H. Yang, "Two-vector-based model predictive torque control without weighting factors for induction motor drives," *IEEE Trans. Power Electron.*, vol. 31, no. 2, pp. 1381–1390, Feb. 2016.
[33] Airbus, *Getting to Grips With Aircraft Performance*. Blagnac, France: Airbus Industrie, 2000.
[34] S. Bozhko, S. Dymko, S. Kovbasa, and S. M. Peresada, "Maximum torque-per-amp control for traction IM drives: Theory and experimental results," *IEEE Trans. Ind. Appl.*, vol. 53, no. 1, pp. 181–193, Jan. 2017.
[35] F. Wang, S. Li, X. Mei, W. Xie, J. Rodrłguez, and R. M. Kennel, "Model-based predictive direct control strategies for electrical drives: An experimental evaluation of PTC and PCC methods," *IEEE Trans. Ind. Informat.*, vol. 11, no. 3, pp. 671–681, Jun. 2015.
[36] H. B. Shin and J. G. Park, "Anti-windup PID controller with integral state predictor for variable-speed motor drives," *IEEE Trans. Ind. Electron.*, vol. 59, no. 3, pp. 1509–1516, Mar. 2012.

Liming Yan was born in Shaanxi, China, in 1988. He received the B.S. degree in software engineering from Chang'an University, Xi'an, China, in 2011, and the M.S. degree in electric machine and electric apparatus from Shenyang University of Technology, Shenyang, China, in 2014. He is currently working toward the Ph.D. degree in electrical engineering at Northwestern Polytechnical University, Xi'an, China.

His research interests include model predictive control of power electronics and electrical drives.

Manfeng Dou (M'08) received the M.S. and Ph.D. degrees in electrical engineering from Northwestern Polytechnical University (NPU), Xi'an, China, in 1991 and 1998, respectively.

He is currently a Professor with NPU. In addition, he is currently the Vice-Director of the Institute of Rare Earth Permanent Magnet (REPM) Electric Machine and Control Technology, NPU. His research interests include electrical machine design, analysis of electromagnetic fields, motion control technology, and intelligent control.

Dr. Dou received the second prize for the China National Invention Award in 1993, the second prize for the China National Defense Science and Technology Progress Award in 2007, and the Youth Science Award of Shaanxi Province, China, in 2004.

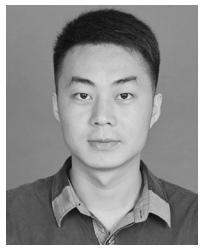

Zhiguang Hua was born in Henan, China, in 1990. He received the Bachelor's degree in electrical engineering from Xi'an University of Technology, Xi'an, China, in 2015.

He is currently a master of electric machine and electric apparatus at Northwestern Polytechnical University, Xi'an, China. His current research interests include motor drive and control, and electromagnetic field analysis of motor.

Haitao Zhang was born in Shanxi, China, in 1988. He received the B.S. and M.S. degrees in electrical engineering, in 2009 and 2012, respectively, from Northwestern Polytechnical University, Xi'an, China, where he is currently working toward the Ph.D. degree in electrical engineering.

From 2012 to 2015, he worked at Bosch Rexroth, Xi'an, China. His research interests include optimum design and control of permanent magnet brushless dc motor.

Jianwei Yang was born in Shanxi, China, in 1986. He received the B.S. degree in electrical engineering in 2009 from Xi'an Technological University, Xi'an, China, and the M.S. degree in power electronics and power drives from Northwestern Polytechnical University, Xi'an, China, in 2012. He is currently working toward the Ph.D. degree in electrical engineering, Northwestern Polytechnical University.

His research interests include sensorless control for electrical drives and fault-tolerant control.